Latin American Journal of Solids and Structures
www.lajss.org

Design of the austempering heat treatment of a ductile iron differential case aided by computer simulation

Abstract
Austempered ductile iron is frequently employed in the fabrication of automobile parts due to its good mechanical properties, and its simplicity and low cost of the manufacturing process. The heat treatment design is an important stage, in which parameters such as temperatures and durations are chosen according to the required microstructure, part dimension, and initial characteristics of ductile iron. A coupled thermo-mechanical-metallurgical model is employed in this work to facilitate the heat treatment design of a ductile iron differential case. The thermal-mechanical model is solved by using a general-purpose software, and the metallurgical model is implemented into it by means of user-defined subroutines. To perform the austempering heat treatment simulation of the part, experimental results were required to complete some basic parameters of the model. In order to select appropriated values of thermal cycle parameters, the numerical model was employed to analyze the influence of austenitizing temperature, and austempering time and temperature in the microstructure, dimensional change of the part, cooling rate, and minimum required time of the heat treatment to obtain a full ausferritic matrix. A good performance of the computational tool was found by comparison of numerical and experimental results.

Keywords
Ductile iron differential case, Austempering heat treatment design, Thermo-mechanical-metallurgical analysis, Finite element analysis.

Adrián D. Boccardo[a,b,*]
Patricia M. Dardati[b]
Luis A. Godoy[a,c]
Juan J. Lopensino[b]

[a]Instituto de Estudios Avanzados en Ingeniería y Tecnología, IDIT, CONICET-Universidad Nacional de Córdoba, Córdoba, Argentina. E-mail: aboccardo@frc.utn.edu.ar

[b]Grupo de Investigación y Desarrollo en Mecánica Aplicada, GIDMA, Facultad Regional Córdoba, Universidad Tecnológica Nacional, Córdoba, Argentina. E-mail: pdardati@gmail.com, lopensino@gmail.com

[c]Facultad de Ciencias Exactas, Físicas y Naturales, Universidad Nacional de Córdoba, Córdoba, Argentina. E-mail: luis.godoy@unc.edu.ar

*Corresponding author

http://dx.doi.org/10.1590/1679-78254559

Received: September 29, 2017
In Revised Form: December 07, 2017
Accepted: December 08, 2017
Available Online: February 02, 2018

1 INTRODUCTION

Austempered Ductile Iron (ADI) is a Fe-C-Si alloy that is frequently used in powertrain and suspension systems of automobiles due to its good mechanical properties, such as $900-1600\,MPa$ tensile strength, $650-1300\,MPa$ yield strength, $1-9\,\%$ elongation, $20-100\,J$ impact energy, and $269-512\,HBW$ hardness (ASTM A 897M-03, 2003). There are also advantages in the manufacturing process to obtain parts having complex shapes (Gundlach and Janowak, 1983; Sorelmetal, 1998; Putman and Thomson, 2003; Mendez *et al.*, 2015). In different types of automobile applications, ADI has been employed to replace cast steel (such as in a spring [illegible] n (crankshaft), because this material allowed weight reduction and cost savings (Sorelmetal, 1998).

The ADI microstructure is formed by graphite nodules embedded into an ausferritic matrix. The ausferritic matrix is composed by sheaves and austenite blocks, and each sheaf is formed by ferrite platelets and austenite films (Sorelmetal, 1998). Parts with this microstructure are commonly obtained by a three-step austempering heat treatment, which is performed in the best case scenario after the casting and machining processes are completed. In the first step of this heat treatment the part is heated and kept at the austenitizing temperature (T_γ). During the second step, the part is cooled and kept at the austempering temperature (T_A). Finally, in the third step the part is cooled to the ambient temperature (Fraś *et al.*, 2012). The described thermal cycle is characterized by the temperature and duration of the first (t_γ) and second (t_A) steps (Sorelmetal, 1998).

The heat treatment temperatures vary in the range of $850°C < T_\gamma < 950°C$ and $250°C < T_A < 450°C$, and the chosen values depend on the desired final microstructure (Bosnjak *et al.*, 2001; Yescas, 2003), which is closely related to the required values of mechanical properties. Appropriate values of t_γ and t_A have to be chosen to obtain ADI parts with a full ausferritic matrix, which depend on some characteristics such as the initial microstructure and chemical composition of ductile iron, and the geometry of the parts (Moncada and Sikora, 1996; Sosa *et al.*, 2004; Sosa *et al.*, 2009; Fraś *et al.*, 2012).

The design process of heat treatment, which allows selecting the thermal cycle parameters, can be aided by numerical simulation, in order to reduce the number and complexity of experimental tests. Computational tools have been successfully employed in different problems of the automotive industry (Kokkula *et al.*, 2006; Lee *et al.*, 2016; Kong *et al.*, 2016). However, this is not a simple problem and to perform an appropriate representation of the phenomena involved in the heat treatment, a coupled thermo-mechanical-metallurgical model is required. The thermal model should allow computation of the evolution of temperature in the part taking into account the latent heat at phase change, the mechanical model is required to compute the evolution of deformation due to temperature and phase changes, whereas the metallurgical model should predict the evolution of phases during the heat treatment development.

Only a few works are found in the literature that consider coupled models for the austempering heat treatment simulation. Yoo *et al.* (1999) proposed a thermo-metallurgical model to simulate the in-situ austempering heat treatment. The metallurgical model allows to predict a ferritic-pearlitic-ausferritic matrix at ambient temperature. The pearlitic and ausferritic transformations are modeled by means of Avrami equation; the model is difficult to employ because the parameters of the equation need to be fitted based on a large number of experiments. In the works of Pérez Villalobos *et al.* (2011) and Hepp *et al.* (2012), the modeling of the austempering heat treatment of ADI parts was presented. Even though the models employed in these works predict the evolutions of temperature and phases in a part, they do not consider microstructural features such as the shape and size of phases and the chemical composition of phases. Moreover, information regarding model application, such as part modeling (initial and boundary conditions, domain discretization) and metallurgical model setting (employed data base or fitting technique) is rather scarce. Boccardo *et al.* (2017b) proposed a thermo-mechanical-metallurgical model for the three-step austempering heat treatment, considering the reverse eutectoid, ausferritic, and martensitic transformations; the modeling involved the microscale in order to consider the microstructure features of the ductile iron, such as graphite nodule size, shape and dimension of the growing phases, heterogeneous carbon concentration within the matrix, among others. This model allows predicting a final martensitic-ausferritic matrix and the final dimensional change of the part.

The aim of the present work is to design the austempering heat treatment of a differential case, which was originally made of an as-cast ductile iron. In order to do that, the general-purpose software ABAQUS is employed to solve the thermal and mechanical problems at a macroscale by means of the finite element method. The metallurgical problem is solved by taking into account the microscale features of the material by a novel model previously published and validated by the authors (Boccardo *et al.*, 2017b), which is here implemented into ABAQUS and coupled with its thermo-mechanical model by means of user-defined subroutines.

The main characteristics of the thermo-mechanical-metallurgical model and the implementation of the metallurgical model into ABAQUS are described in Section 2. In Section 3 the modeling of the differential case is developed. Moreover, the strategy to fit the metallurgical model by means of simple and standard experimental tests is included. Numerical results obtained for different values of heat treatment parameters are presented and discussed in Section 4. Finally, conclusions are drawn about the computational tool employment, fitting process of the metallurgical model, and the obtained thermal cycle, dimensional changes, and microstructure.

2 NUMERICAL MODEL

The numerical tool used in this work is a coupled thermo-mechanical-metallurgical model. It allows computing the evolution of the microstructure as a function of the temperature and, in turn, the evolution of the temperature as a function of the phase changes. Moreover, the model predicts the evolution of deformations due to temperature and phase changes. The thermal and mechanical problems are solved at the macroscale, whereas the evolution of the microstructure is predicted by means of a model developed at microscale. The temperature, deformation, and microstructure characteristics are calculated in the whole part.

2.1 Thermo-mechanical model

A coupled temperature-displacement transient analysis was performed in this work using ABAQUS under small deformation assumptions (ABAQUS, 2010).

For the mechanical model, the constitutive response of the ductile iron was modeled assuming an elasto-plastic behavior with isotropic hardening according to the J2-flow theory of plasticity. Furthermore, this behavior was considered to be temperature-dependent. Based on the work of Boccardo *et al.* (2017b), the relation between the stress σ and total strain e is given by the constitutive law defined as:

$$\sigma = C:(e - e^{p} - e^{v}) \tag{1}$$

where C is the temperature-dependent isotropic elastic constitutive tensor, e^{p} is the plastic strain tensor, and e^{v} is the strain tensor associated to a volume expansion or contraction due to temperature and phase changes.

The von Mises yield function is assumed to represent the plastic behavior of the ductile iron (Celentano *et al.*, 2013):

$$f = (3J_2)^{(1/2)} - (C_o + C_h) \tag{2}$$

where J_2 is the second invariant of the deviatoric part of σ, $C_h = A\left(e^{p}_{eq}\right)^{n}$ is the isotropic plastic hardening function (where A is the strength index, n is the strain hardening exponent, and e^{p}_{eq} is the equivalent plastic deformation), and C_o is the temperature-dependent yield strength defining the initial elastic boundary.

It is assumed that temperature and phase changes generate an isotropic volume deformation at the macroscale. The volume deformation is evaluated by employing the model proposed by Christien *et al.* (2013), which is based in the variation of the microstructure density. The increment of the strain tensor Δe^{v}, required by the ABAQUS formulation, is evaluated as:

$$\Delta e^{v} = \frac{\rho^{mic}_{o}}{3}\left(\frac{\rho^{mic}_{t-\Delta t} - \rho^{mic}_{t}}{\rho^{mic}_{t-\Delta t}\rho^{mic}_{t}}\right)1 \tag{3}$$

where ρ^{mic}_{o}, $\rho^{mic}_{t-\Delta t}$, and ρ^{mic}_{t} are the microstructure density at beginning of the simulation (reference state), at time $t-\Delta t$, and at time t. Moreover, 1 is the unit tensor of second-rank.

The microstructure density varies with both temperature and phase changes; and it is evaluated by means of the rule of mixtures:

$$\rho^{mic}_{i} = \sum f_{ph}\rho_{ph} \tag{4}$$

where f_{ph} and ρ_{ph} are the volume fraction and density of the microconstituents, respectively. The phase volume fractions are computed with the metallurgical model described in Section 2.2. The temperature-dependent phase densities are calculated as in Boccardo *et al.* (2017b).

For the thermal problem, the heat released or absorbed by phase change is considered (Boccardo *et al.*, 2017b). The heat transfer equation is written as follows:

$$\rho c\frac{\partial T}{\partial t} = div\left(Kgrad(T)\right) + \dot{Q} \tag{5}$$

where T is the temperature, t is the time, ρ is the density, c is the specific heat capacity, $\dot{Q}$ is the thermal power released or absorbed by phase changes, and K is the isotropic conductivity tensor of second-rank defined as $K = k1$, where k is the conductivity. The material parameters c and k are considered temperature-dependent.

In order to simulate the heat transfer between the part and the environment, a boundary condition based on Newton's law was imposed at the part/environment interface (Boccardo *et al.*, 2017b):

$$q_{conv} = -h\left(T - T_{env}\right) \tag{6}$$

where q_{conv} is the normal heat flux, h is the heat transfer coefficient at interface, and T and T_{env} are the temperatures at both sides of the interface.

The initial condition applied to the entire domain is $T = T_o$, where T_o is a uniformly distributed temperature.

2.2 Metallurgical model

The metallurgical model simulates the microstructure evolution during the three-step of the austempering heat treatment. The metallurgical model considers an initial microstructure formed by ferritic, ferritic–pearlitic, or pearlitic matrices. During the heat treatment the microstructure suffers several phase transformations.

The model considers the development of:

- Stable (EITs) and metastable (EITm) reverse eutectoid transformations, in which ferrite and pearlite transform into austenite, respectively, during the heating from ambient temperature up to austenitizing temperature.
- Austenite carbon homogenization (ACH) during which the austenite carbon concentration is homogenized at austenitizing temperature.
- Ausferritic transformation (AT) in which austenite transforms into ferrite platelets during the cooling from austenitizing temperature down to ambient temperature. In the development of this transformation the ausferritic matrix is obtained.
- Martensitic transformation (MT) in which austenite transforms into martensite during the cooling from austenitizing temperature down to ambient temperature.

The solution scheme of the metallurgical model is illustrated in Figure 1, where TEITs, TEITm, TAT, and TMT are the temperatures at which transformations EITs, EITm, AT, and MT start, respectively; additionally, f_{Gr} and f_{γ} are the graphite and austenite volume fractions, respectively. Notice that the developments of phase changes depend on the value of temperature and the microstructure at time t.

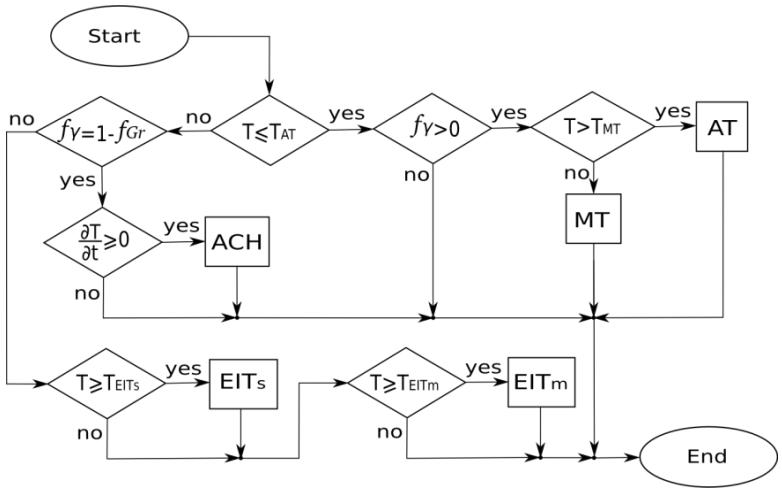

Figure 1: *Metallurgical model: Schematic representation of the resolution (Boccardo et al., 2017b).*

The microscale metallurgical model represents the evolution of the phases by means of representative volume elements that allow considering microstructure characteristics such as the type, shape, and size of phases that form the ductile iron. The graphite nodules are assumed as spheres which are grouped into sets according to their radii; the number of sets is denoted as $nsetsg$. Additionally, the pearlite colonies are considered as a laminated composite of cementite and ferrite layers and they are grouped into $nsetsc$ sets according to their interlaminar spacing. The equations to compute the volume fractions of graphite nodules, austenite, ferrite platelets, and martensite are (Boccardo *et al.*, 2017b):

$$f_{Gr} = \frac{4}{3}\pi \sum_{i=1}^{nsetsg} \left(N_{set_i} r_{Gr_i}^3 \right) \tag{7}$$

$$f_\gamma = \begin{cases} \dfrac{4}{3}\pi \displaystyle\sum_{i=1}^{nsetsg}\left[N_{set_i}\left(r_{\gamma_i}^3 - r_{Gr_i}^3\right)\right] + \sum_{j=1}^{nsetsc}\left[f_{p_j}^o \dfrac{\left(x_{\gamma_j} - x_{\theta_j}\right)}{x_{\alpha_j}}\right] & \text{for EIT} \\ \dfrac{4}{3}\pi \displaystyle\sum_{i=1}^{nsetsg}\left[N_{set_i}\left(r_{shell_i}^3 - r_{Gr_i}^3\right)\right] & \text{for ACH} \\ \dfrac{4}{3}\pi \displaystyle\sum_{i=1}^{nsetsg}\left\{N_{set_i}\left[r_{shell_i}^3\left(1 - f_{\alpha p_i}\right) - r_{Gr_i}^3\right]\right\} & \text{for AT} \\ f_{\gamma b}^o\left[1 - f_{(\gamma b \to m)}\right] + f_{\gamma shell}^o\left[1 - f_{(\gamma shell \to m)}\right] & \text{for MT} \end{cases} \tag{8}$$

$$f_{\alpha p} = \frac{4}{3}\pi \sum_{i=1}^{nsetsg}\left(f_{\alpha p_i} N_{set_i} r_{shell_i}^3\right) \tag{9}$$

$$f_m = f_{(\gamma b \to m)} f_{\gamma b}^o + f_{(\gamma shell \to m)} f_{\gamma shell}^o \tag{10}$$

where r_{Gr}, r_γ, and r_{shell} are the radii of graphite nodule, austenite that grows within ferrite, and the spherical representative volume elements employed for ACH and AT, respectively; x_θ, x_γ, and x_α are the coordinates of cementite-austenite and austenite-ferrite interfaces, and the length of the unidimensional representative element employed for EITm. Moreover, f_p^o is the initial volume fraction of pearlite, $f_{\gamma b}^o$ and $f_{\gamma shell}^o$ are the volume fractions of austenite block and austenite shell at the beginning of MT, $f_{\alpha p}$ is the volume fraction of ferrite platelets, while $f_{(\gamma b \to m)}$ and $f_{(\gamma shell \to m)}$ are the volume fractions of austenite block and austenite shell that transform into martensite, respectively. Finally, N_{set} is the number of graphite nodules per unit of volume. The factors affected by subscripts i and j are related to the sets of graphite nodules and pearlite colonies, respectively.

The kinetics of phase transformation is computed by means of ordinary differential equations that are solved numerically with the explicit Euler method. The model employed for the ausferritic transformation simulates the nucleation of ferrite platelets by an incubation time function. This exponential function, Equation 11, has two parameters (k_1 and k_2) that need to be fitted with experimental data for each chemical composition of ductile iron (Boccardo *et al.*, 2017a).

$$t_{inc} = \frac{k_1}{\nu_f}\exp\left[\frac{k_2}{RT}\left(1 + \frac{\Delta G_m}{k_3}\right)\right] \tag{11}$$

where ΔG_m is the maximum free energy available for nucleation at paraequilibrium condition, ν_f is the attempt frequency factor, R is the gas constant, k_1 and k_2 are empirical parameters to be fitted, and $k_3 = 2540 J/mol$.

Once the model is fitted correctly for a chemical composition, it is able to represent the evolution of ferrite platelets for other values of graphite nodule count and austempering temperature. A full description and equations of the employed metallurgical model has been presented by Boccardo *et al.* (2017b).

2.3 Metallurgical model implementation

The metallurgical model was implemented and coupled to the thermo-mechanical model of ABAQUS using user-defined subroutines that were written in Fortran (ABAQUS, 2010). These subroutines allow to extend the functionality of ABAQUS with modules defined by the user.

The USDFLD subroutine is used to implement the metallurgical model represented in Figure 1. Thus, the metallurgical model is solved at material points (Gauss points) of each finite element of the thermo-mechanical model. The variables related to the phase evolutions are stored into the STATEV array (solution-dependent state variables array) and it allows to pass information to HETVAL subroutine and visualize the results at the postprocess. The temperature within USDFLD is obtained by GETVRM subroutine.

The variables of the metallurgical model placed into STATEV array are initialized, at the beginning of the simulation, by employing the SDVINI subroutine. This subroutine also provides a check point to the input data. If problems are detected during the checking process, the calculation is stopped by STDB_ABQERR subroutine and a suitable error message is generated.

The heat flux generation $\dot{Q}$ due to phase changes is computed by HETVAL subroutine, and it is calculated as follows (Stefanescu, 2009):

$$\dot{Q} = \rho\left(L_{\alpha\to\gamma}\frac{\partial f_{\gamma_s}}{\partial t} + L_{p\to\gamma}\frac{\partial f_{\gamma_m}}{\partial t} + L_{\gamma\to\alpha}\frac{\partial f_{\alpha p}}{\partial t} \right) \tag{12}$$

where $L_{\alpha\to\gamma}$, $L_{p\to\gamma}$, and $L_{\gamma\to\alpha}$ are the latent heats of EITs, EITm, and AT transformations, respectively. Moreover, f_{γ_s} and f_{γ_m} are the austenite volume fractions formed during EITs and EITm, respectively. Volume fraction derivatives are numerically evaluated.

The model to evaluate the deformations due to temperature and phase changes, Equation 3, is implemented into ABAQUS by means of the UEXPAN subroutine.

3 DIFFERENTIAL CASE MODELING

The austempering heat treatment of the differential case was performed in this paper by means of computer simulation. The specific part of interest is a gearbox component of front wheel drive automobiles.

The initial microstructure of the whole part is composed by graphite nodules embedded into a ferritic-pearlitic matrix as shown in Figure 2. The graphite nodule count per unit of area is $200 nod/mm^2$, and the volume fractions of graphite, ferrite, and pearlite are 0.16, 0.64, and 0.2, respectively, which were determined by image analysis of optical micrographs. The chemical composition, which is a design constraint, is 3.4C-0.8Mn-0.03Cr-0.4Cu-2.3Si-Fe (in weigh percent).

In order to select appropriated values of the heat treatment parameters, several simulations were performed varying the austenitizing temperature, and austempering time and temperature.

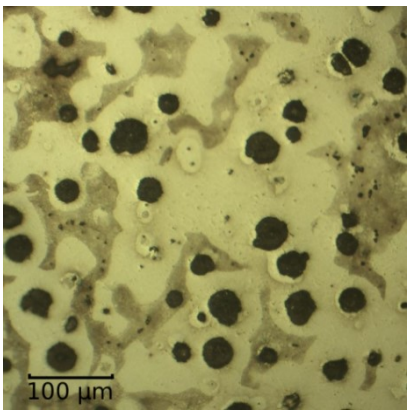

Figure 2: *Initial microstructure of the part. Graphite nodules in black, pearlite in brown, and ferrite in white.*

3.1 Modeling of the part

The geometry was model in 3D, Figure 3a, and the domain was discretized with 109,605 tetrahedron elements of 4 nodes (C3D4T), as shown in Figure 3b. The number of elements was determined by means of a convergence analysis. The initial temperature was set as $T_o = T_{Amb}$, being the ambient temperature $T_{Amb} = 20°C$, and

the convection boundary condition was applied at the external surfaces of the geometry. The heat transfer coefficient depends on the type of environment, and it was set as $h = 70 W/\left(m^2\,°C\right)$ during all the heating (furnace) and the cooling from T_A down to T_{Amb} (room at ambient temperature), whereas $h = 400 W/\left(m^2\,°C\right)$ during the cooling from T_γ down to T_A (salt bath) (Boccardo *et al.*, 2017b). The thermal and mechanical properties of ductile iron are shown in Tables 1 and 2, respectively.

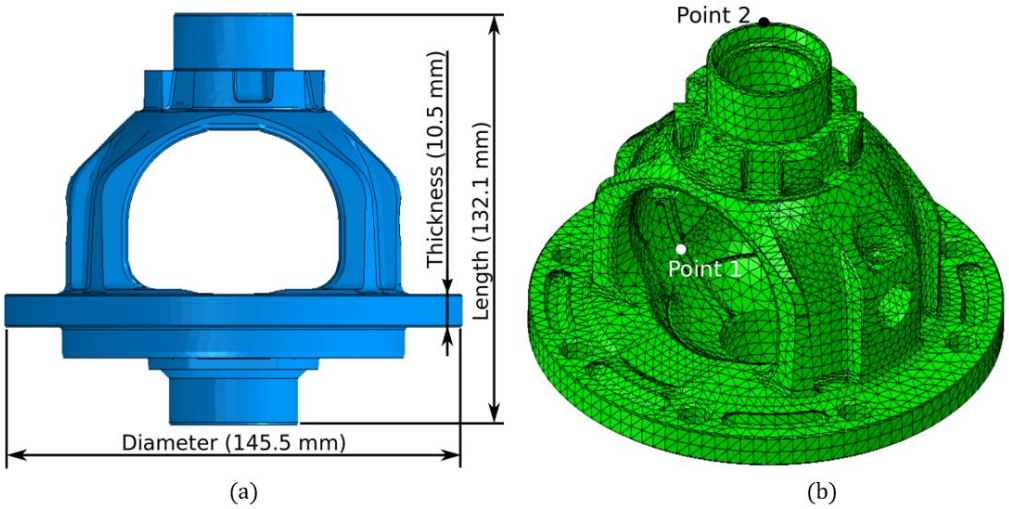

Figure 3: *(a) geometry and (b) 3D mesh of the part.*

Table 1: *Thermal properties of ductile iron (Lacaze and Gerval, 1998; Kapturkiewicz et al., 2005; Celentano et al., 2013).*

Temperature $\left[°C\right]$	Conductivity $\left[W/\left(m°C\right)\right]$	Specific heat $\left[J/\left(kg°C\right)\right]$
20	44.1	500
280	44.1	612
420	40.9	672
560	37.1	732
700	33.6	750
840	28.1	758
980	22.5	786
$\rho = 7000 kg/m^3$		
Latent heat $\left[J/kg\right]$: $L_{\alpha\to\gamma} = 5.8\times10^4$		
$L_{p\to\gamma} = 1.28\times10^4$ $L_{\gamma\to\alpha} = 5.8\times10^4$		

Table 2: *Mechanical properties of ductile iron (Celentano et al., 2013).*

Temperature $[°C]$	Young's Modulus $[MPa]$	Yield strength $[MPa]$
20	163,471	260
100	163,113	255
200	160,174	250
300	151,650	230
400	135,276	210
500	110,898	135
600	81,386	60
700	52,021	50
720	46,668	48
750	44,267	45
770	43,788	42
800	44,356	40
830	45,935	37
850	42,935	35
900	35,435	30
1000	28,435	20
Poisson's ratio: $\upsilon = 0.33$		
Hardening parameters: $A = 300 MPa$, $n = 0.22$		

The metallurgical model was solved by considering graphite nodules of equal radius and pearlite colonies of equal interlaminar spacing ($nsetsg = 1$ and $nsetsc = 1$). The graphite nodule count per unit of volume was calculated as $N_{set_1} = 3/4\left(\pi NA_{set_1}^3\right)^{1/2}$ (Boccardo *et al.*, 2017a), where $NA_{set_1} = 200 nod/mm^2$, and the interlaminar spacing of pearlite was set to 0.5×10^{-5} (coarse pearlite). The parameters of the ausferritic transformation model are obtained using the fitting process described in Section 3.2.

3.2 Model fit

As described in the previous section, the ausferritic transformation model has two parameters to be fitted (k_1 and k_2). The fitting strategy employed requires both experimental tests and numerical simulations, and it allows the model to consider the variation of the austempering temperature when the graphite nodule count remains constant.

Fourteen cuboid samples of small dimensions ($20 mm \times 10 mm \times 5 mm$) were extracted of one differential case, see Figure 4, and subjected to an experimental austempering heat treatment, all of them were austenitized at $T_\gamma = 950°C$ during $t_\gamma = 1200 s$, while the values of T_A and t_A were varied, as is shown in Table 3 and Figure 5, in order to characterize the kinetics of the ausferritic transformation for two different values of austempering temperature. The three steps of the heat treatment were developed into a small laboratory furnace, a molten salt bath (sodium nitrate and sodium carbonate with 1:1 ratio), and a room at ambient temperature.

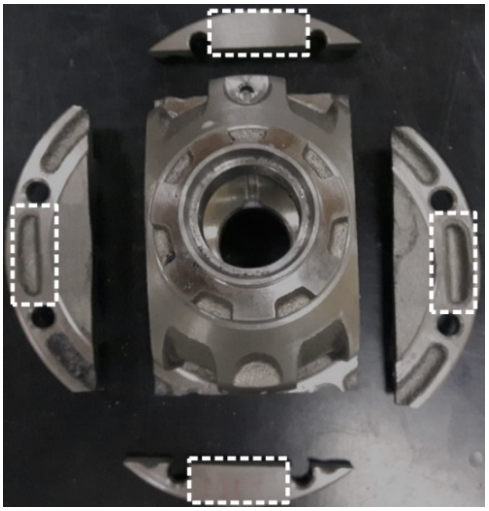

Figure 4: *Regions of which small samples were extracted (Regions indicated in dash line).*

After the heat treatment, the samples were polished and etched during $15 s$ with Picral reactive ($4\ \%$ picric acid in ethyl alcohol) to reveal the sheaves formed during the ausferritic transformation. Alternatively, Lepera's reactive ($1\ \%$ aqueous solution of sodium metabisulfite and $4\ \%$ picral (LePera, 1980)) was employed, and similar results were reached. The micrographs obtained for 370_1 and 370_4 samples are presented in Figure 6. Then, volume fractions of sheaves were measured by means of image analysis. As shown in Figure 7a for both values of austempering temperature, the microstructure presented an ausferritic-martensitic matrix at lower austempering time (small sheaves volume fraction) and a full ausferritic matrix at higher time.

Additionally, Brinell hardness measurement was performed using $10 mm$ steel ball and $3000 kgf$. As shown in Figure 7b, the hardness decreases as austempering time increases, because sheaves volume fraction increases (or martensite volume fraction decreases).

Table 3: *Temperatures and times employed for the second step.*

Sample	$T_A\ [°C]$	$t_A[s]$
300_1	300	900
300_2		2100
300_3		3000
370_1	370	420
370_2		840
370_3		1380
370_4		2640

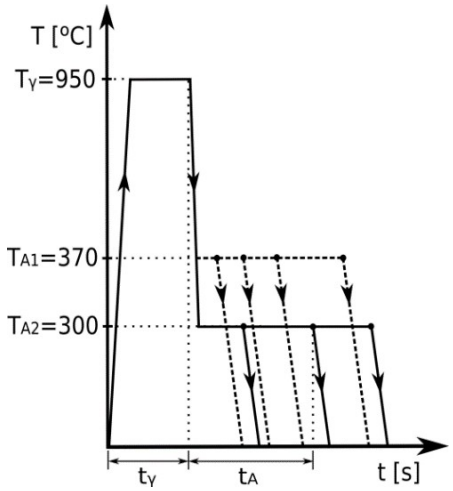

Figure 5: *Thermal cycle of small samples employed to characterize the kinetics of the ausferritic transformation.*

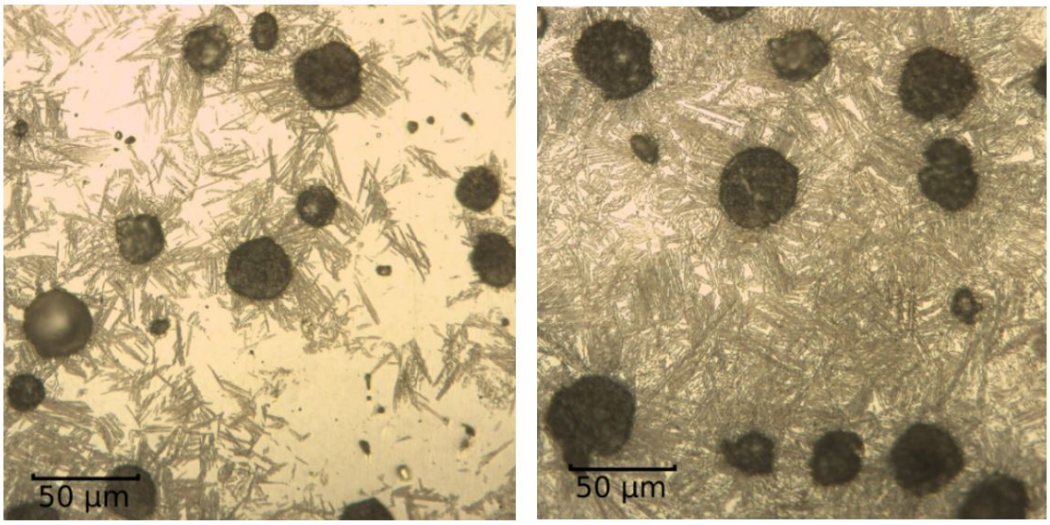

Figure 6: *Final microstructure of small samples austemperized at* $T_A = 370°C$ *for: (a)* $t_A = 420s$ *and (b)* $t_A = 2640s$ *. Graphite nodules in black, sheaves in brown, and austenite/martensite in white.*

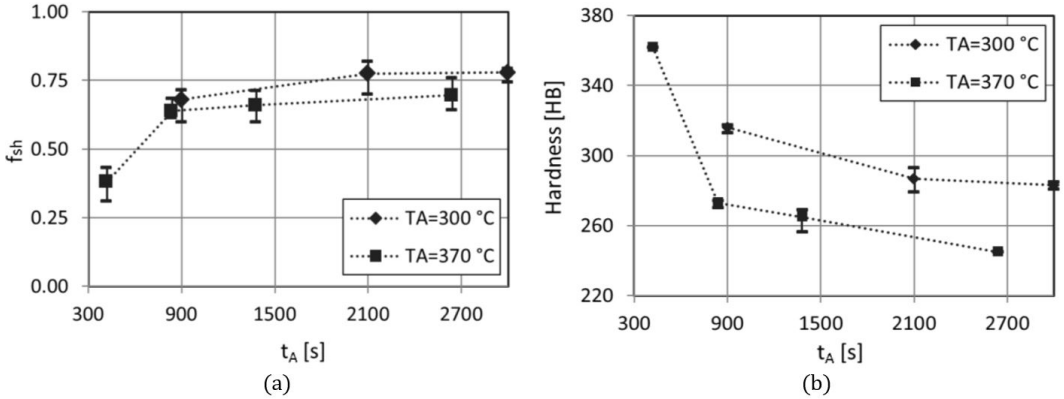

Figure 7: *Evolution of: (a) sheaves volume fraction and (b) hardness, with austempering time and temperature.*

Finally, the parameters k_1 and k_2 were obtained by fitting the model response to the experimental results. In order to do that, the thermo-mechanical-metallurgical model was employed to simulate the heat treatment of

300_3 and 370_4 samples for different combinations of k_1 and k_2. The geometry was meshed using 1950 tetrahedron elements of 4 nodes (C3D4T) and the convection boundary condition was applied at the external surfaces of the geometry. The optimal combination of these parameters minimizes the sum of the square differences between numerical and experimental results, being the employed results the normalized sheaf volume fraction (f_n). This sum takes into account the mentioned difference of the two specimens used in the fitting process.

The values obtained of the parameters were $k_1 = 3.5087 \times 10^{14}$ and $k_2 = 1.9671 \times 10^4 \, J/mol$. In Figure 8 the results of the simulations employing these fitted values are compared with experiments for both austempering temperatures.

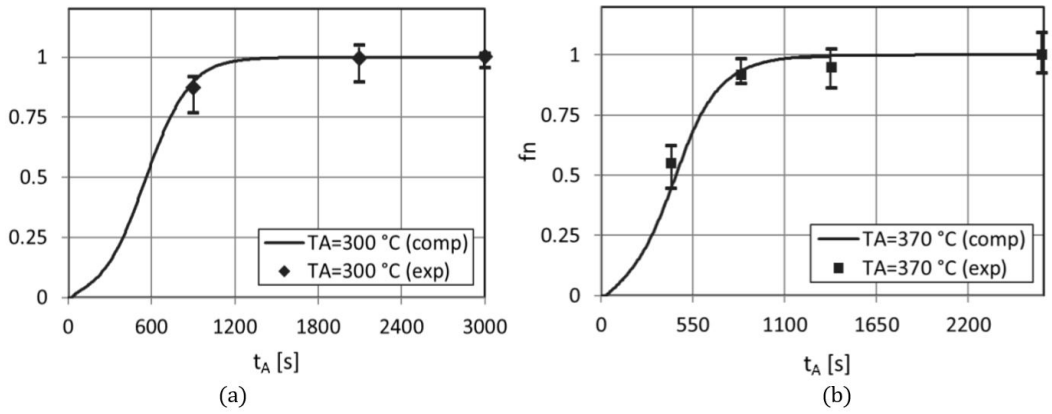

Figure 8: *Kinetics of ausferritic transformation employing the fitted values of* k_1 *and* k_2 *for: (a)* $T_A = 300°C$ *and (b)* $T_A = 370°C$.

4 RESULTS AND DISCUSSION

The evolutions of temperature, phase volume fractions, and dimensional change of the differential case length during the heat treatment simulation were analyzed for $T_\gamma = 950°C$, $T_A = 330°C$, and $t_A = 2700s$.

In Figure 9a the temperature evolutions at points 1 and 2 of the part, see Figure 3b, are compared. Even though these points presented the largest difference in temperature evolution, it was small. In the first step, the variation of temperature evolution caused by the heat absorption of reverse eutectoid transformation was observed in the region A. Regarding phase evolutions, Figure 9b, during the first step the austenite volume fraction increased up to its maximum value (0.925) due to both reverse eutectoid transformation and austenite carbon homogenization. The volume fraction of this phase decreased during the second step as a consequence of the ausferritic transformation, in which it was consumed by ferrite platelets. The ausferritic transformation ended at $T_A = 330°C$, but it restarted during the cooling down to the ambient temperature, a fact that explains the changes in austenite and ferrite platelet volume fractions as is shown in the figure. According to the numerical simulation, there was no martensite formation. The predicted evolution of austenite and ferrite platelets is in agreement with the experimental observations reported by Fraś *et al.* (2012). The length dimensional change during the heat treatment was studied, which is defined as $DC = \left(m_t - m_o\right)/m_o$, where m is the value of the dimension, and the subscripts o and t stand for the initial value and the value at time t, respectively. At the end of the first step an increment of the part length was observed, Figure 9c. This dimensional change had the contribution of both temperature increment, which produced an expansion, and phase change, which produced a contraction as may be observed in region A. At the beginning of the second step the length reduction occurred due to cooling from T_γ down to T_A, followed by an expansion caused by the austempering transformation, see region B. Finally, the length was decreased in the third step as a consequence of the cooling down to ambient temperature.

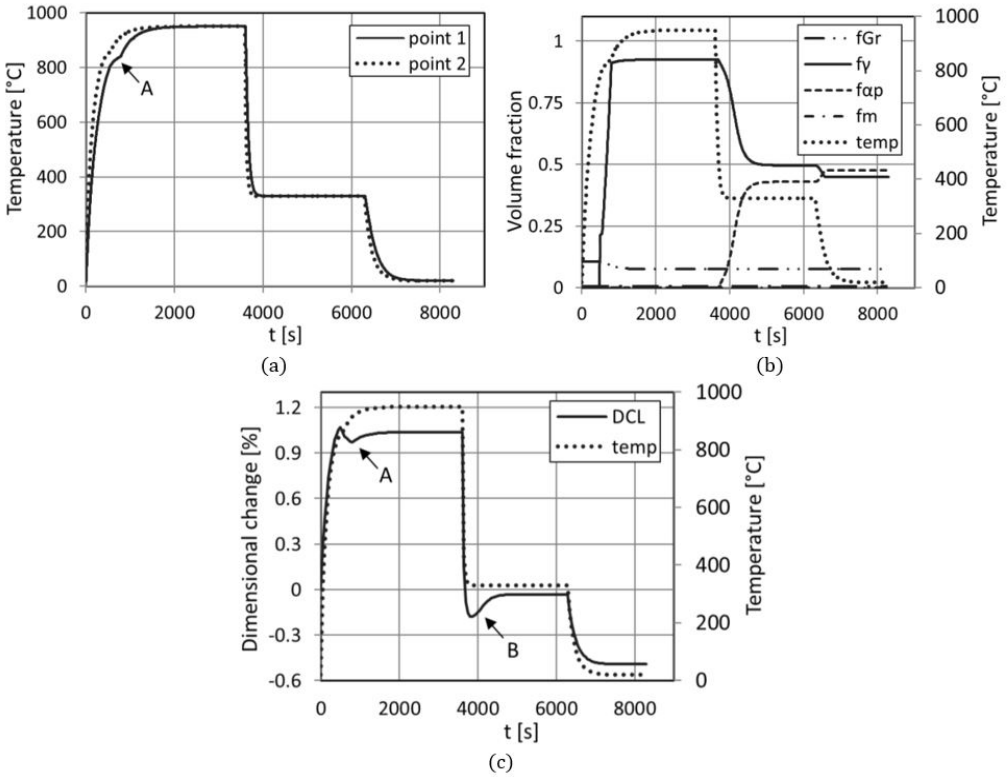

Figure 9: *Numerical results: (a) evolutions of temperatures at points 1 and 2 of the part, (b) evolutions of phase fractions at point 1, and (c) evolution of length dimensional change.*

Figure 10 presents the ferrite platelet and austenite volume fractions at the end of the simulated heat treatment. The values of these fractions, in the whole part, are almost uniform and around of $f_{\alpha p} = 0.475$ and $f_{\gamma} = 0.45$. For each phase, the small difference occurred due to different cooling rates during the cooling from T_A down to T_{Amb}.

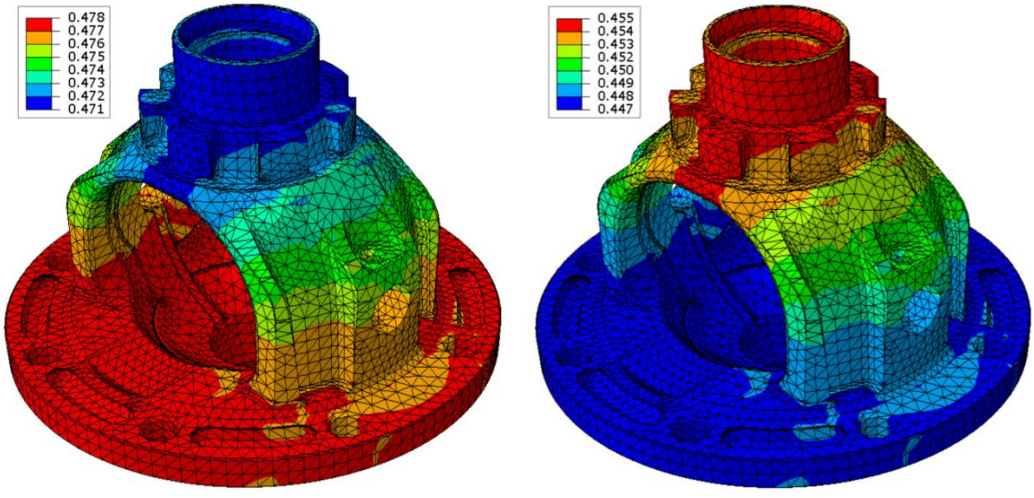

Figure 10: *Predicted volume fractions, at the end of the heat treatment, of: (a) ferrite platelets and (b) austenite.*

4.1 Influence of austempering time

The influence of austempering time in the final microstructure and final dimensional change of diameter (DCD), thickness (DCT), and length (DCL), see Figure 3a, was studied. Several heat treatment simulations were performed for $T_\gamma = 950°C$, $T_A = 330°C$, and austempering time in the range of $180 \leq t_A \leq 3600 s$. The final phase volume fractions, for each austempering time, were almost uniform in the whole part and their average values are presented in Figure 11a. For austempering time less than $1000 s$ a final ausferritic-martensitic matrix was predicted by the model. The martensite volume fraction decreased when the austempering time increased. To obtain a full ausferritic matrix with a maximum ferrite platelet volume fraction, the austempering time has to be greater than $2400 s$, which is the required time to end the ausferritic transformation at T_A. It is worthwhile to notice that the same behavior was observed in samples employed to fit the metallurgical model. The dimensional change at the end of the heat treatment is defined as $DC = \left(m_f - m_o\right)/m_o$, where m is the value of the dimension, and the subscripts o and f stand for the initial and final values, respectively. As is shown in Figure 11b, dimension reductions occurred for any austempering time. The maximum reduction occurred for the maximum ferrite platelet volume fraction, which is obtained when the ausferritic transformation has been completely developed at T_A. Moreover, DCD, DCT, and DCL were very close each other, because the final volume fraction is almost uniform in the whole part.

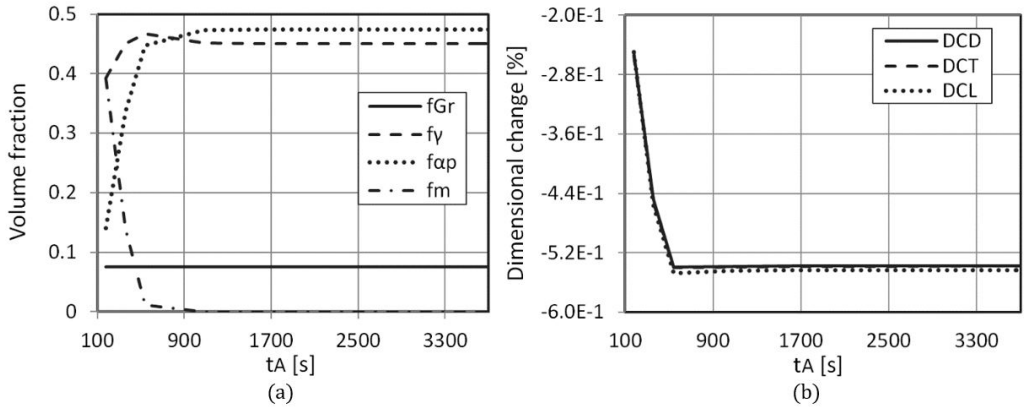

Figure 11: *Numerical results of the influence of austempering time in: (a) final phase fractions and (b) final dimensional change of diameter, thickness, and length.*

4.2 Influence of austenitizing and austempering temperatures

The influence of austenitizing and austempering temperatures in the minimum required time for both first and second steps, final microstructure, final dimensional change, and cooling rate during the cooling from T_γ down to T_A was studied. Simulations were performed for austenitizing and austempering temperatures in the ranges of $880°C \leq T_\gamma \leq 950°C$ and $300°C \leq T_A \leq 400°C$.

The minimum required time for the first step (t_γ^{min}) has the contribution of a) time to get the temperature at which the reverse eutectoid transformation starts and b) time to transform the initial microstructure. In the simulation it was observed that when T_γ increased, the first time is increased and the second one decreased. The resulting variation of t_γ^{min} with T_γ is shown in Figure 12a, and the maximum difference was $2.6\,\%$. On the other hand, the minimum required time for the second step (t_A^{min}) has the contribution of a) time to get the temperature at which the ausferritic transformation starts and b) time to transform the austenitic matrix into an ausferritic one. The maximum and minimum values of the first time were obtained at $T_\gamma = 950°C$ - $T_A = 400°C$ and

$T_\gamma = 880°C$ - $T_A = 300°C$, respectively; meanwhile the maximum and minimum values for the second one were obtained at $T_\gamma = 950°C$ - $T_A = 300°C$ and $T_\gamma = 880°C$ - $T_A = 400°C$, respectively. The resulting variation of t_A^{min} with T_γ and T_A is shown in Figure 12b, and the maximum difference was $9.7\,\%$.

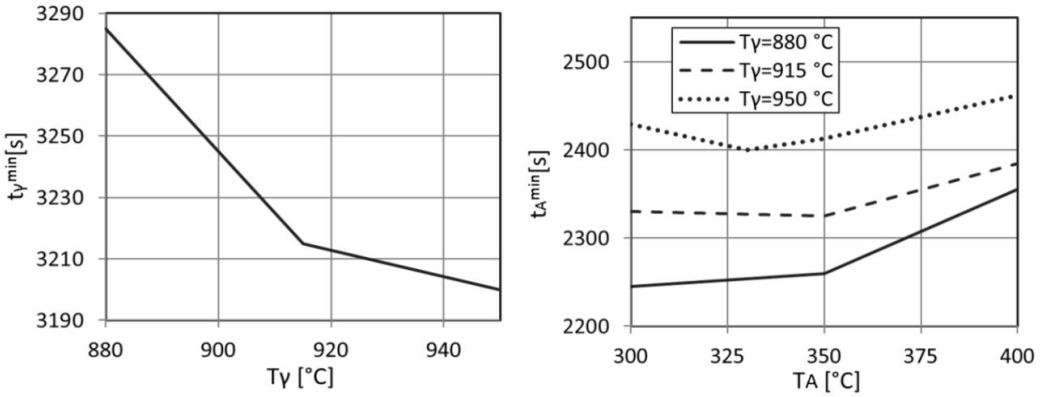

(c) (b)

Figure 12: *Numerical results of the influence of: (a) austenitizing temperature in the minimum required time for the first step and (b) austenitizing and austempering temperatures in the minimum required time for the second step.*

Regarding the microstructure at the end of the heat treatment, the graphite volume fraction depended on the austenitizing temperature, decreasing its fraction with the increment of the temperature, as may be seen in Figure 13a. The maximum difference in the graphite volume fraction was $9.3\,\%$. The ferrite platelet volume fraction increased with the decrement of both T_γ and T_A, therefore the maximum volume fraction was obtained at $T_\gamma = 880°C$ - $T_A = 300°C$, and the maximum difference was $16.3\,\%$, as is shown in Figure 13b. The variation of this phase fraction with T_A was less than the expected, because a large amount of ferrite platelets was formed during the third step when the part was cooling from a high value of T_A. The behavior of austenite volume fraction was opposite to the found for the ferrite platelets, because austenite was consumed by the second phase during the ausferritic transformation.

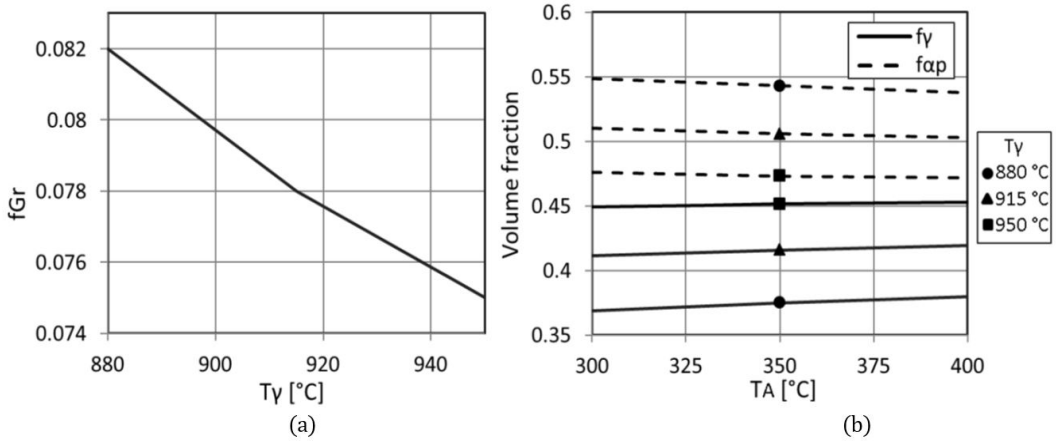

(a) (b)

Figure 13: *Numerical results of the influence of: (a) austenitizing temperature in the final graphite volume fraction and (b) austenitizing and austempering temperatures in the final ferrite platelet and austenite volume fractions.*

The final dimensional change of diameter, thickness, and length of the part are presented in Figure 14 for different values of austenitizing and austempering temperatures. As mentioned in Section 4.1, DCD, DCT, and DCL

dimensional changes were very close to each other, because the final volume fraction is almost uniform in the whole part. Moreover, the dimensional changes were highly influenced by T_γ, being the maximum difference of $30\ \%$.

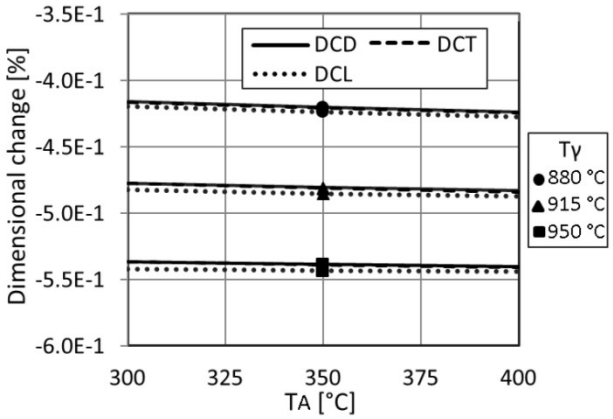

Figure 14: *Numerical results of the influence of austenitizing and austempering temperatures in the final dimensional change of diameter, thickness, and length.*

In order to obtain a full ausferritic matrix, the eutectoid transformation has to be avoided (transformation of austenite into ferrite and pearlite). One way to do that is by subjecting the part to high cooling rate during the cooling from T_γ down to T_A (Venugopalan, 1990). In Figure 15 the cooling rate at point 1, developed between $880°C$ and $600°C$, is presented for different values of T_γ and T_A. The analysis is presented for this part point, because it presented the lowest value of cooling rate. The cooling rate is defined as $CR = (800-600)°C/\Delta t$, where Δt is the required time to cool the part from $880°C$ to $600°C$. As may be seen, the cooling rate increased when T_γ increased and T_A decreased, and the maximum difference was $38.6\ \%$.

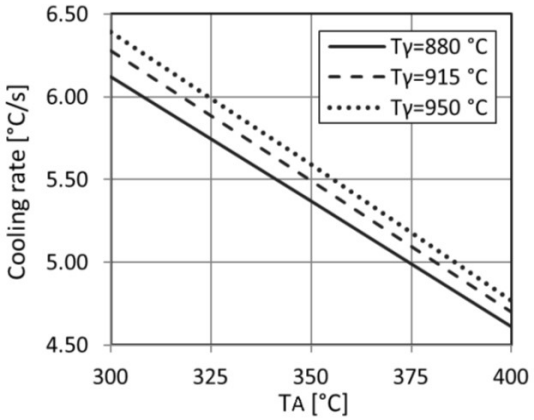

Figure 15: *Numerical results of the influence of austenitizing and austempering temperatures in the cooling rate, at point 1, during the cooling of the second step.*

4.3 Influence of size and geometry of the part

The size and geometry of the differential case is a design constraint. However, in order to analyze how the heat treatment is developed in parts with different size and geometry, the numerical results of both differential case (DFC) and small sample employed to fit the model (SS) were compared. The heat treatment simulations were performed for $T_\gamma = 950°C$ and $T_A = 330°C$.

A small difference was observed in the final microstructure. The ferrite platelet volume fraction in DFC was $4\,\%$ greater than for SS, because different amount of this phase was formed during the cooling from T_A down to ambient temperature. As a consequence the final dimensional change (in absolute value) in SS is $3\,\%$ greater than for DFC.

The minimum required time for the first step was highly influence by the size and geometry, being $1130\,s$ and $3200\,s$ for SS and DFC, respectively. As was mentioned in Section 4.2, t_γ^{min} has the contribution of a) time to get the temperature at which the reverse eutectoid transformation starts and b) time to transform the initial microstructure. In SS these contributions were smaller than for DFC. The minimum required time for the second step was $2335\,s$ and $2400\,s$ for SS and DFC, respectively, indicating that it was slightly influenced by the mentioned changes. The small difference occurred because a different time was necessary to get the temperature at which the ausferritic transformation starts, due to different cooling rate for SS ($21.05°C/s$) and DFC ($5.91°C/s$) during the cooling down to T_A, and that the duration of the ausferritic transformation at T_A was almost the same for both parts.

4.4 Selection of heat treatment parameters

As shown in Sections 4.1 and 4.2, the austenitizing temperature, the austempering temperature, and the austempering time highly influence the final phase fraction, final dimensional change, among other variables.

In order to obtain a final microstructure composed by graphite nodules and a full ausferritic matrix, the duration of the second step is chosen to be equal to t_A^{min}. The selected values for the temperatures are $T_\gamma = 950°C$ and $T_A = 330°C$ because they allow to obtain: (a) the desired microstructure for the part application and (b) high cooling rate that prevents the transformation of austenite into ferrite and pearlite. For the chosen temperatures, the minimum required time for first and second steps are $t_\gamma^{min} = 3200\,s$ and $t_A^{min} = 2400\,s$. The final dimensional change, due to the heat treatment, has to be considered in both pre and post machining processes in order to satisfy the dimensional tolerance.

The differential case was heat treated in a laboratory in order to verify the results obtained with the simulation. The durations chosen for the first and second steps were around 10% greater than the durations predicted by the model ($t_\gamma = 3600\,s$ and $t_A = 2700\,s$), and the experimental procedure was the same that the employed for the small samples.

As was predicted by the simulation, the microstructure obtained in the experiment is uniform in the whole part. The presence of ferrite, pearlite, and martensite was not observed, as is shown in Figure 16, even in the region with the lowest cooling rate from T_γ to T_A (point 1).

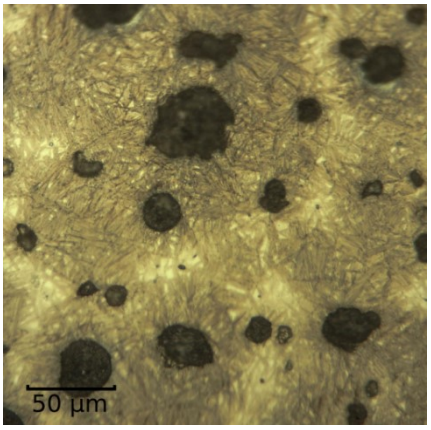

Figure 16: *Final microstructure of the differential case at point 1, which presents a full ausferritic matrix. Graphite nodules in black, sheaves in brown, and austenite in white.*

5 CONCLUSIONS

The design of the austempering heat treatment of a ductile iron differential case, aided by computer simulation, was presented in this paper. The simulation was performed with a coupled thermo-mechanical-metallurgical model, which was fitted to the chemical composition of the part.

The main conclusions drawn from the work may be summarized as follows:

(a) The metallurgical model was implemented into ABAQUS by means of user-defined subroutines. The pre-process, resolution, and post-process required to perform the simulations and analyses of results were carried out in spite of the complexity of the part geometry and the large size of the employed finite element mesh.

(b) The metallurgical model was successfully fitted to the alloy chemical composition by employing a standard procedure that involved experimental heat treatment, at different austempering times and temperatures, and microstructure analysis of several small samples obtained of one differential case.

(c) According to the simulations, the austempering time modifies the type of final microstructure. In the differential case, ausferritic-martensitic and ausferritic matrices are obtained for short and large values of austempering times, respectively. The same behavior is observed in the samples employed to fit the metallurgical model. Additionally, the austenitizing temperature highly influences the final phase volume fraction (decrement of graphite and ferrite platelet volume fractions with a temperature increment) and final dimensional change (increment of the contraction with a temperature increment) when the ausferritic transformation was completely developed at the austempering temperature.

(d) The minimum time required for the first step of the differential case heat treatment is influenced by the austenitizing temperature (decrement of this time with a temperature increment). On the other hand, when the size of the part is reduced, the minimum required time decreases. The minimum required time for the second step of the differential case heat treatment is influenced by the austenitizing and austempering temperatures in a not simple way, and it suffers a small variation when the size of the part is reduced.

(e) The temperature evolution in whole part presented small differences; a fact that allowed to obtain a uniform ausferritic matrix, at the end of the heat treatment, in the whole part.

(f) The model was appropriate to predict the minimum required time, for both first and second steps, to obtain a full ausferritic matrix at the end of the heat treatment. The predicted values were $t_{\gamma}^{min} = 3200\,s$ and $t_{A}^{min} = 2400\,s$, and the experimental heat treatment of the part was developed increasing both t_{γ} and t_{A} in 10%.

(g) Amounts of ferrite and pearlite were not observed in the micrographs of the treated differential case, indicating that the cooling rate was correctly chosen. The cooling rate highly depends on the austempering temperature. When considerable amounts of ferrite and pearlite are obtained during the cooling from austenitizing temperature down to austempering temperature, the metallurgical model has to consider the development of the eutectoid transformation in order to represent adequately the phase evolution throughout the three-step austempering heat treatment.

Acknowledgment

During the course of this Research A.D. Boccardo had a postdoctoral scholarship from CONICET. L.A. Godoy is a member of the research staff of CONICET. This work was supported by a grant from Universidad Tecnológica Nacional (ASUTNCO0004735). The experimental heat treatment was developed at Departamento de Ingeniería Metalúrgica, Facultad Regional Córdoba, Universidad Tecnológica Nacional. The authors thank the contributions of Diego J. Celentano in the development of some parts of the model reported in this paper.

References

ABAQUS (2010). ABAQUS documentation, version 6.10, Dassault Systèmes, Providence, RI, USA.

ASTM A 897M-03 (2003). Standard specification for austempered ductile iron castings.

Boccardo, A., Dardati, P., Celentano, D., Godoy, L. (2017a). A microscale model for ausferritic transformation of austempered ductile irons. Metallurgical and Materials Transactions A 48:524-535.

Boccardo, A., Dardati, P., Celentano, D., Godoy, L. (2017b). Austempering heat treatment of ductile iron: Computational simulation and experimental validation. Finite Elements in Analysis and Design 134:82-91.

Bosnjak, B., Radulovic, B., Pop-Tonev, K., Asanovic, V. (2001). Influence of microalloying and heat treatment on the kinetics of bainitic reaction in austempered ductile iron. Journal of Materials Engineering and Performance 10(2): 203-211.

Celentano, D., Dardati, P., Carazo, F., Godoy, L. (2013). Thermomechanical-microstructural modelling of nodular cast iron solidification. Materials Science and Technology 29:156-164.

Christien, F., Telling, M., Knight, K. (2013). A comparison of dilatometry and in-situ neutron diffraction in tracking bulk phase transformations in a martensitic stainless steel. Materials Characterization 82:50-57.

Fraś, E., Górny, M., Tyrała, E., Lopez, H. (2012). Effect of nodule count on austenitising and austempering kinetics of ductile iron castings and mechanical properties of thin walled iron castings. Materials Science and Technology 28(12):1391-1396.

Gundlach, R.B. and Janowak, J.F. (1983). Development of a ductile iron for commercial austempering. AFS Transactions 86:377.

Hepp, E., Hurevich, V., Schäfer, W. (2012). Integrating modeling and heat treatment simulation of austempered ductile iron. IOP Conference Series: Materials Science and Engineering 33:012076.

Kapturkiewicz, W., Fraś, E., Burbelko, A. (2005). Computer simulation of the austenitizing process in cast iron with pearlitic matrix. Materials Science and Engineering A 413-414:352-357.

Kokkula, S., Langseth, M., Hopperstad, O.S., Lademo, O.G. (2006). Behaviour of an automotive bumper beam-longitudinal system at 40% offset impact: an experimental and numerical study. Latin American Journal of Solids and Structures 3:59-73.

Kong, Y.S., Abdullah, S., Omar, M.Z., Haris, S.M. (2016). Topological and topographical optimization of automotive spring lower seat. Latin American Journal of Solids and Structures 13:1388-1405.

Lacaze, J. and Gerval, V. (1998). Modelling of the eutectoid reaction in spheroidal graphite Fe-C-Si alloys. ISIJ International 38:714-722.

Lee, S., Kim, B., Lee, H.-J., Yoon, J. (2016). Warm forging of an aluminium alloy for the differential case in an automobile transmission. Proceedings of the Institution of Mechanical Engineers, Part D: Journal of Automobile Engineering 230(8):1131-1139.

LePera, F. (1980). Improved etching technique to emphasize martensite and bainite in high-strength dual-phase steel. Journal of Metals 32:38-39.

Mendez, S., de la Torre, U., Larranaga, P., Suarez, R., Stefanescu, D. (2015). New as-cast ductile iron raises bar properties. Metal Casting Design & Purchasing 17(5):39-44.

Moncada, O.J. and Sikora, J.A. (1996). Dimensional change in austempered ductile iron. AFS Transactions 104:577-580.

Pérez Villalobos, I., Getzlaff, U., Köser, O. (2011). Predicción mediante la simulación de la microestructura en fundiciones ADI tras el tratamiento térmico. FundiPress: Revista de la Fundición 28:30-33.

Putman, D. and Thomson, R. (2003). Microstructural and mechanical property modelling of austempered ductile iron. International Journal of Cast Metals Research 16:191-196.

Sorelmetal (1998). Ductile iron data for design engineers, Rio Tinto Iron & Titanium Inc. (Montreal).

Sosa, A.D., Echeverría, M.D., Moncada, O.J. (2004). Machining and heat treatment effects on distortion and residual stresses in an industrial application of ADI. ISIJ International 44(7):1195-1200.

Sosa, A.D., Echeverría, M.D., Moncada, O.J., Míngolo, N., Sikora, J.A. (2009). Influence on nodule count on residual stresses and distortion in thin wall ductile iron plates of different matrices. Journal of Materials Processing Technology 209:5545-5551.

Stefanescu, D. (2009). Science and engineering of casting solidification, 2nd ed., Springer (New York).

Venugopalan, D. (1990). Computer modeling of ferrite and pearlite formation in ductile iron. Physical Metallurgy of Cast Iron IV: Proceedings of the Fourth International Symposium on the Physical Metallurgy of Cast Iron 271-278.

Yescas, M. (2003). Prediction of the vickers hardness in austempered ductile irons using neural networks. International Journal of Cast Metals Research 15:513-521.

Yoo, S.M., Moeinipour, K., Ludwig, A., Sahm, P.R. (1999). Numerical simulation and experimental results of in situ heat treated austempered ductile iron. International Journal of Cast Metals Research 11:483-88.